Association of SPIN90, Arp2/3 complex, and formin mDia1 controls cortical actin organization

Luyan Cao[1]*, Amina Yonis[2,3]*, Malti Vaghela[2,4]*, Elias H Barriga[3,12], Priyamvada Chugh[5], Matt Smith[5,13], Julien Maufront[6,7], Geneviève Lavoie[8], Antoine Méant[8], Emma Ferber[2], Miia Bovellan[2,3], Art Alberts[9,†], Aurélie Bertin[6,7], Roberto Mayor[3], Ewa K. Paluch[5,10,14], Philippe P. Roux[8,11], Antoine Jégou[1,#], Guillaume Romet-Lemonne[1,#], Guillaume Charras[2,3,10,#]

1. Université de Paris, CNRS, Institut Jacques Monod, 75013 Paris, France
2. London Centre for Nanotechnology, University College London, WC1H 0AH, UK
3. Department of Cell and Developmental Biology, University College London, WC1E 6BT, UK
4. Department of Physics and Astronomy, University College London, WC1E 6BT, UK
5. MRC-Laboratory for Molecular Cell Biology, University College London, WC1E 6BT, UK
6. Laboratoire Physico Chimie Curie, Institut Curie, PSL Research University, CNRS UMR168, 75005 Paris, France
7. Sorbonne Universités, 75005 Paris, France
8. Institute for Research in Immunology and Cancer, Université de Montréal, Montréal, Canada
9. Van Andel research institute, Grand Rapids, MI, USA
10. Institute for the Physics of Living Systems, University College London, WC1E 6BT, UK
11. Department of Pathology and Cell Biology, Université de Montréal, Montréal, Canada

Present addresses:

12. Instituto Gulbenkian de Ciência, 2780-156 Oeiras, Portugal.
13. The Francis-Crick institute, London, UK
14. Physiology, Development and Neuroscience, University of Cambridge, Cambridge, UK

† Deceased

*Equal contribution

#Equal contribution

Authors for correspondence: Guillaume Charras (g.charras@ucl.ac.uk), Guillaume Romet-Lemonne (romet@ijm.fr) and Antoine Jégou (antoine.jegou@ijm.fr).

Lead contact: Guillaume Charras

Summary

Cellular shape is controlled by the submembranous cortex, an actomyosin network mainly generated by two actin nucleators: the Arp2/3 complex and the formin mDia1. Changes in relative nucleator activity may allow cells to rapidly alter their cortical organization, mechanics and shape but how this is controlled is unknown. Here, we investigate how nucleation-promoting factors (NPFs) mediate interaction between nucleators. In vitro, the NPF SPIN90 promotes formation of unbranched filaments by Arp2/3, a process thought to provide the initial filament for generation of dendritic networks. Paradoxically, in cells, we find that SPIN90 appears to favor a formin-dominated cortex. Our experiments *in vitro* reveal this feature stems mainly from two mechanisms: efficient recruitment of mDia1 to SPIN90-Arp2/3 nucleated filaments and formation of a ternary SPIN90-Arp2/3-mDia1 complex that greatly enhances filament nucleation. Both mechanisms yield rapidly elongating filaments with mDia1 at their barbed ends and SPIN90-Arp2/3 at their pointed ends. Thus, in networks, SPIN90 lowers branching densities and increases the proportion of long filaments elongated by mDia1. This synergistic interplay between Arp2/3 and mDia1 may regulate the diverse actin structures present in cells.

Introduction

One of the most striking properties of living cells is their ability to change shape during physiological processes, such as division, migration, and differentiation. Cellular shape changes are governed by mechanical changes in the cortex, a thin network of actomyosin below the membrane[1]. Changes in cortical mechanics can originate from changes in myosin activity[2] or cortex architecture, which arise from changes in actin filament length[3] or network organization[4]. One potential mechanism to control cortex architecture involves regulation of actin nucleators. Indeed, *in vitro,* in the presence of profilin, formins generate longer filaments than those created by Arp2/3-mediated branching[5,6] and, in cells, single molecule experiments suggest a similar trend[7]. Furthermore, actin nucleators can generate varied network topologies ranging from highly branched networks generated by the Arp2/3 complex to linear arrays generated by formins and Ena/VASP. This suggests that a switch in the dominant F-actin nucleator might also alter F-actin network organization. However, little is known about how nucleator activity is controlled to change network topology and mechanics.

Many cellular actin-based structures such as the cortex, the leading edge of migrating cells, phagocytic cups, and intercellular junctions require both formins and the Arp2/3 complex for their formation[8-12]. This is surprising because the actin networks they generate differ extensively in their topology, protein interactors, dynamics, and force generation[4,11,13,14]. Some reports have shown synergistic action of pointed end nucleators (such as Spire or APC) with barbed end nucleators (such as formins)[15-17], whereas others have shown sequential action of nucleators[18]. Overall, these observations underscore the importance of nucleator crosstalk for the generation of functionally optimal actin structures in cells.

In addition to RhoGTPases, ancillary proteins, known as Nucleation Promoting Factors (NPFs), are also involved in activating nucleators or maintaining their activity[19]. Arguably, the best studied NPF is the Wave regulatory complex (WRC), which consists of five subunits (SRA1, NAP1, Abi1, BRK1, WAVE2) and activates the Arp2/3 complex to generate branched actin networks[19]. After the Wave complex detaches from Arp2/3, another NPF, cortactin, stabilizes Arp2/3 attachment to mother filaments against debranching[19]. Some NPFs have been reported to interact with multiple nucleators, making them prime candidates to mediate interplay. IQGAP1 can maintain the activity of mDia1 via its C-terminal DBR domain (**Fig 1A**) but also promote Arp2/3 activity by interacting with N-WASp and the Wave complex via its N-terminal Calponin Homology Domain (CHD)[20-22]. Another NPF, SPIN90/DIP/WISH/NCKIPSD, has been reported to interact with Arp2/3 in some studies and formins in others. SPIN90 forms a complex with Arp2/3 by binding to the region that interacts with the side of mother filaments[23] and, as a result, it stimulates formation of unbranched filaments[24]. In addition to kickstarting the generation of branched networks by providing the initial filament necessary for subsequent branching mediated by the WRC and Arp2/3[23], very recent work proposes that SPIN90 competes with the WRC to modulate the degree of branching in networks[25]. Furthermore, SPIN90 can interact with the diaphanous related formins (DRF) mDia1 and mDia2 via its LRR and/or SH3 domains (**Fig 1A**)[26,27] and, surprisingly, it inhibits actin filament elongation by mDia2 but not mDia1[26].

Here, we examine how NPFs regulate nucleator activity in the sub-membranous actin cortex to control its organization, assembly kinetics, and mechanics. We show that IQGAP1 controls the activity of the formin mDia1 and WRC regulates Arp2/3 branching activity. Furthermore, we demonstrate that SPIN90 mediates an unexpected synergistic action between Arp2/3 complex and mDia1.

Results

Several NPFs localize to the actin cortex

Previous proteomic analyses revealed the presence of two actin nucleators in the cortex of M2 blebbing melanoma cells, the Arp2/3 complex and the formin mDia1, which were found responsible for nucleating the bulk of the actin cortex in M2 and HeLa cells[9]. Several NPFs that could regulate these nucleators were also present (**Fig 1B**): the Wave Regulatory Complex, IQGAP1, cortactin, SPIN90, and Fli-1 (protein flightless-I homolog, an NPF that binds to the DAD domain of formins to prevent autoinhibition[28]). Published proteomic datasets indicate that these NPFs are also expressed in HeLa cells (Table S1), suggesting they may play a general role in controlling cortical nucleator activity[29-31].

We examined NPF localization in M2 melanoma cell blebs and metaphase HeLa cells. Blebs provide a snapshot into the cortex life cycle[32], while mitosis represents a key physiological function of the cortex. All NPFs identified in proteomics localized to the cortex of mitotic HeLa cells and retracting blebs, where a cortex reforms *de novo* by nucleation (**Fig 1C,D** and **S1A-D**). Thus, the NPFs identified by proteomics are promising candidates for coordinating the activity of cortical nucleators.

We concentrated on WRC and SPIN90 because they mediate the transition from branched to unbranched actin networks nucleated by Arp2/3, and IQGAP1 and SPIN90 because they may coordinate the activity of Arp2/3 and mDia1.

SPIN90 depletion mimics mDia1 depletion and increases bleb size

To determine how NPFs modulate nucleator activity, we examined their effect on bleb size in M2 cells knowing that Arp2/3 depletion results in small blebs, whereas mDia1 depletion results in large blebs[9]. As expected, IQGAP1 depletion resulted in more cells with large blebs (**Fig 1E, G, S1E,S1G**), consistent with a role in maintaining mDia1 activity[20], and depletion of the WRC subunits gave a small bleb phenotype (**Fig 1F-G, S1E, S1H-I**), consistent with the well-established role of WRC in regulating Arp2/3 (**Fig 1F-G**). Surprisingly, SPIN90 depletion resulted in a large bleb phenotype (**Fig 1E, G, S1E-F**), suggesting that SPIN90 cooperates with mDia1 directly or indirectly rather than inhibiting DRF formins as previously reported[26]. These unexpected results (summarized in **Fig S2**) led us to focus on SPIN90.

SPIN90 depletion perturbs cell proliferation

Previous work showed that mDia1 depletion increased cell death, whereas Arp2/3 depletion did not[9]. When we examined the impact of NPF depletion on proliferation in HeLa cells, we found that depletion of WRC subunits did not increase cell death, similar to depletion of Arp2/3 complex, and IQGAP1 depletion led to a two-fold increase in cell death (**Fig 1H-I, S3**). This latter effect was likely mediated by interaction between mDia1 and IQGAP1 because expression of the mouse IQGAP1 DBR domain in IQGAP1-depleted cells decreased cell death to near baseline levels (**Fig 1A,J**). Like mDia1 depletion, SPIN90 depletion increased cell death three-fold, SPIN90 again appearing to cooperate with mDia1 rather inhibiting it (**Fig 1I, S3**). We confirmed the specificity of depletion by expressing full-length mouse SPIN90 in SPIN90-depleted cells (**Fig 1J**). Examination of changes in mRNA transcript abundance by qPCR confirmed that the effect of SPIN90 and IQGAP1 depletion was not due to indirect regulation of NPFs or nucleators at the transcriptional level (**Fig S4**). Thus, mDia1 activity regulated by IQGAP1 and SPIN90 is necessary for proliferation (**Fig S2**).

SPIN90 depletion decreases cortical mesh size in blebs

We then we examined how NPF depletion affects the organization of F-actin in the cortex of M2 cell blebs. Previous work showed that depletion of mDia1 led to large gaps within the cortex, while Arp2/3 depletion led to no clear change in actin filament density[9]. IQGAP1 depletion led to a two-fold increase in the proportion of gaps with diameters larger than 140nm in the cortex (**Fig 2A-B, S5**), similar to the

effect of mDia1 depletion. NAP1 depletion did not significantly change gap diameter distribution or network organization, similar to ACTR2 depletion (**Fig 2A,B, S5**). SPIN90 depletion led to a visibly denser cortex (**Fig 2A**) and a 20% increase in the proportion of gaps less than 30nm in diameter (**Fig 2B, S5**). This was surprising because previous cell-scale assays showed that SPIN90 depletion phenocopied mDia1 depletion (**Fig 1**) and may result from SPIN90's function as an Arp2/3 activator. Indeed, SPIN90 has been proposed to compete with WRC for Arp2/3 to regulate the degree of branching[25]. Depletion of SPIN90 would therefore lead to a denser cortical network because of increased branching. This scenario would suggest the existence of competition between SPIN90 and the WRC-induced branching for Arp2/3 and, along with our previous results (**Fig 1**), would also imply that mDia1 alone is an inefficient nucleator, consistent with *in vitro* experiments[6]. Thus, SPIN90 may mediate crosstalk between mDia1 and Arp2/3 (**Fig S2**).

SPIN90 depletion increases cortical actin density and decreases cortical thickness in mitotic cells

We next determined if NPF depletion affected cortical thickness and cortical density during mitosis in HeLa cells by analyzing the fluorescence profile of an F-actin fluorescent reporter with respect to the plasma membrane (**Fig 2C**)[33]. Previous work has shown that depletion of mDia1 leads to a decrease in cortical thickness whereas depletion of Arp2/3 does not affect thickness[3]. Depletion of IQGAP1 and NAP1 had no impact on cortical thickness or density (**Fig 2D, 2E**). As for mDia1 depletion[3], depletion of SPIN90 significantly decreased cortical thickness by ~25% (**Fig 2D**). However, SPIN90 depletion also led to a ~50% increase in cortex density (**Fig 2E**), something not observed with mDia1 depletion[3] but consistent with the decrease in cortical gap size measured by SEM (**Fig 2A-B**).

Together, these results highlight that SPIN90 depletion possesses features distinct from mDia1 depletion (**Fig S2**), suggesting a unique role for SPIN90 in controlling cortex architecture at the molecular-scale.

SPIN90 controls rapid cortical actin accumulation by mDia1 in mitotic cells

To quantitatively examine the role of NPFs in regulating nucleator activity in the cortex, we measured the cortical F-actin accumulation rate in blebs generated by ablation of the cortex of a metaphase HeLa cell using a pulsed UV laser[34] (**Fig 2F, S7A-B).** Previous work showed that mDia1 depletion decreases F-actin accumulation rate, whereas depletion of Arp2/3 subunits increases it[9]. Depletion of IQGAP1 and NAP1 mirrored the respective effects of mDia1 and Arp2/3 depletion, consistent with their proposed roles (**Fig 2H-I**). SPIN90 depletion led to a significant decrease in actin regrowth rate, again arguing for cooperation with mDia1 (**Fig 2G,I**). Together these results indicate that NPFs regulate actin network growth kinetics in the cortex of mitotic HeLa cells (**Fig S2**).

SPIN90 depletion stiffens the mitotic cell cortex

Recent work has shown that modulating nucleator activity affects cell mechanics[2,3,7]. To probe cortical mechanics, we indented rounded metaphase HeLa cells with a blunt AFM tip limiting ourselves to depths of <500nm, where the cortex dominates mechanics[35] (**Fig 2J**). The apparent elasticity determined from these experiments is sensitive to contributions from cortical elasticity (for example because of a change in the mesh size of the cortex) and cortical tension (for example due to a change in filament length distribution[3] or the abundance of cortical myosin[2]).

First, we examined the effect of nucleator inhibition/depletion. Inhibition of formins with SMIFH2 led to a significant decrease in apparent stiffness, consistent with previous results[7] (**Fig 2L)**. However, mDia1 depletion had no effect (**Fig 2L**), perhaps because of a more acute effect of SMIFH2 or a low sensitivity of apparent stiffness to reduction in cortical tension[3]. Inhibition of the Arp2/3 complex with CK666 or depletion with shRNA led to a greater than two-fold significant increase in apparent stiffness

that could be reversed by blebbistatin treatment (**Fig 2K**, **Fig S7E**), consistent with observations that Arp2/3 complex inhibition increases cell contractility[36].

Depletion of NAP1 led to a ~two-fold increase in apparent elasticity, consistent with Arp2/3 depletion (**Fig 2K**) but in contradiction with reports of a decrease in tension for SRA1 depletion[37]. Depletion of IQGAP1 did not change apparent elasticity, similar to mDia1, but surprisingly, SPIN90 depletion led to a ~two-fold increase (**Fig 2L, Fig S2**). Changes in cortical elasticity did not correlate with changes in cortical pMLC abundance (**Fig S6, Fig S2**) or cortical density (**Fig 2E**), suggesting that they stem from complex changes in network organization at the microscale.

SPIN90 is essential for cell division during embryonic morphogenesis

Having shown an unexpected role for SPIN90 in cancer cells, we examined its role in embryonic tissues where cells must frequently divide and change shape for tissue morphogenesis. Previous work has shown roles for the WRC and IQGAP1 during embryonic morphogenesis[38,39] as well as the presence of mDia1 in the gastrula epithelium[40]. We therefore investigated a role for the SPIN90 ortholog in early *Xenopus Laevis* embryos using morpholino injections (**Fig S8, S9**).

SPIN90-depleted embryos initially developed normally but, by stage 9, they displayed epidermal cells many fold larger than in control embryos because they were multinucleated (**Fig 3A-B**), consistent with a role for SPIN90 in cell cycle progression observed in cancer cells (**Fig 1I,J**). This phenotype eventually led to epidermis rupture and embryonic death at gastrulation. The late phenotype onset is perhaps due to reliance on maternal protein prior to mid-blastula transition or to a change in the nucleation pathway for cortical actin after ectoderm specification around stage 7 [41]. Cell enlargement and multi-nucleation could both be rescued by co-injection of full-length mouse SPIN90 (**Fig 3C-D**). Junctional F-actin in SPIN90-depleted embryos at stage 9 appeared separated from the cell membrane (arrows, **Fig 3E**), a phenotype that could also be rescued by co-injection of full-length mouse SPIN90. Thus, SPIN90 is necessary for tissue morphogenesis during early development likely through a role in cell division.

SPIN90 mediates crosstalk between nucleators to control network organization

Thus far, our data indicate that IQGAP1 acts as an NPF for mDia1 and that the WRC acts as an NPF for the Arp2/3 complex (**Fig S2**). Many of the phenotypes linked to SPIN90 depletion suggest that it acts cooperatively with mDia1 (bleb size, cell cycle progression, thickness, actin accumulation rate) and stiffness measurements suggest it acts as an NPF for Arp2/3, while it presents a distinct phenotype in other assays (mesh size, cortical density) (**Fig S2**). As SPIN90 can interact with both nucleators, we examined a role in mediating their crosstalk *in vitro*, using purified proteins.

First, we examined interactions between SPIN90 and each nucleator alone. We confirmed that SPIN90 activates nucleation of filaments by Arp2/3 in a dose-dependent manner (**Fig S10B-C**) and that SPIN90 stays bound in a complex with Arp2/3 at the pointed end of nucleated filaments (**Fig. S11A**)[23]. Nucleation of new filaments by SPIN90-Arp2/3 is not instantaneous, suggesting that Arp2/3 bound to SPIN90 does not instantly behave like an active barbed end (**Fig. S11A**). We also confirmed that SPIN90 can bind to mDia1 without affecting its activity (**Fig. S11B-C and S10D-F**). Therefore, cellular phenotypes suggesting that SPIN90 may act as an activator of mDia1 are not likely due to direct enhancement of mDia1 activity.

We then examined how SPIN90 altered the organization of F-actin networks in a minimal system of purified proteins containing actin, profilin, Arp2/3, VCA (a domain of Wave-2 that activates Arp2/3) and mDia1. In the absence of SPIN90, the nucleation of mother filaments was slow, generating a network that consisted of few very densely branched regions (**Fig 4A**). When SPIN90 was present,

filaments were rapidly nucleated giving rise to a more homogenous network with longer filaments, reminiscent – albeit at a larger length-scale – of the cell cortex architectures observed by electron microscopy (**Fig 2A**) and of the rapid growth observed for mDia1-generated cortices (**Fig 2H-I**).

To further characterize the role of SPIN90, we quantified the number of mother filaments and the branching density as a function of SPIN90 concentration, with and without mDia1. In both situations, SPIN90 greatly increased the nucleation of mother filaments and decreased the density of branches on mother filaments (**Fig 4B-C and Fig S12)**, consistent with the competition with VCA-induced branching for Arp2/3 complexes suggested by others[25]. Overall, adding SPIN90 leads to the formation of more barbed ends, which appear more evenly distributed over the surface (**Fig 4A-C**). The extensive and very localized branching observed in the absence of SPIN90 may explain in part why SPIN90 depletion leads to a denser cortex in cells (**Fig 2A, D**). Due to the presence of profilin in our assay, we can identify filaments with mDia1 at their barbed ends because they elongate rapidly[42]. Consistent with the global increase in the number of barbed ends, SPIN90 strongly increased the density of mDia1-elongated filaments (**Fig 4E**). Strikingly, the fraction of mDia1-bearing barbed ends also grew with increasing concentrations of SPIN90 (**Fig 4F**), suggesting that SPIN90 somehow favors the recruitment of mDia1 to barbed ends.

Collectively, these data show that SPIN90 modulates network organization by shifting the balance of branched to unbranched filaments generated by the Arp2/3 complex and by facilitating the addition of mDia1 to the barbed end to generate long filaments. Importantly, these effects were noticeable at NPF ratios close to those present in cells (**Table S1**).

Barbed ends nucleated by SPIN90-Arp2/3 have an enhanced affinity for mDia1

We hypothesized that mDia1 might have different affinities for barbed ends generated with or without SPIN90. To test this hypothesis, we performed single filament experiments where we observed different types of filaments in the same open chamber. We first compared mDia1's affinity for mother filaments and branches by adding Alexa488-labeled actin, profilin and mDia1 to preformed branched Alexa568-labeled actin filaments (**Fig 5A**). This revealed that mDia1 has the same affinity for the barbed ends of mother filaments and branches. We then compared spontaneously nucleated filaments (preformed using Alexa568-labeled actin) and filaments nucleated by SPIN90 and Arp2/3 (preformed using 15% Alexa488-labeled actin), which we mixed together with 3% Alexa488-labeled actin, profilin and mDia1 (**Fig 5B**). Filaments of each subpopulation were identified by the color and intensity of their pointed end regions. Strikingly, the fraction of mDia1-bearing barbed ends was 38% larger for SPIN90-Arp2/3-nucleated filaments (**Fig 5B, S13A**). This indicates that filaments nucleated by SPIN90-Arp2/3 recruit mDia1 more efficiently to their barbed ends. When we monitored co-existing populations of single filaments in a microfluidics setup, we found that mDia1 has a 2-fold higher affinity for barbed ends nucleated by SPIN90-Arp2/3 than for those nucleated by spectrin-actin seeds (**Fig 5C**). This may explain why some of our cell-scale experiments suggest that SPIN90 could act as an activator of mDia1.

We next asked whether the fraction of mDia1-bearing barbed ends could be further increased if we included mDia1 during nucleation of filaments by SPIN90 and Arp2/3. To do this, we mixed short Alexa568-labeled actin filaments nucleated by SPIN90-Arp2/3 with a solution of Alexa488-labeled actin, profilin, mDia1, Arp2/3 and SPIN90 (**Fig. 5D, S13C**). Control experiments with no SPIN90 showed that nucleation by mDia1 alone was negligible in these conditions (**Fig S13B**). Filaments nucleated by SPIN90-Arp2/3 in the presence of mDia1 had a 53% higher fraction of rapidly growing barbed ends than the pre-nucleated filaments marked by Alexa568. A possible explanation would be that mDia1 has a stronger affinity for shorter, recently nucleated filaments. As this does not appear to be the case

(**Fig S13D**), we hypothesized that SPIN90-Arp2/3 recruits mDia1 to nucleate a rapidly growing filament.

SPIN90 forms a ternary complex with the Arp2/3 complex and mDia1 to nucleate fast growing filaments

To test the existence of a ternary complex, we performed GST pull-down experiment by decorating GST beads with SPIN90 and pre-incubating them with various concentrations of Arp2/3 before incubation with mDia1 (Supplementary Methods). While SPIN90-decorated beads were able to recruit mDia1 in the absence of Arp2/3, the amount of mDia1 increased with increasing Arp2/3 complex present on the beads (**Fig 6A**, **S11C, S15A**). This indicates that mDia1 binds to the SPIN90-Arp2/3 complex with a higher affinity than to SPIN90 alone. In addition, although it was reported previously that SPIN90 can interact with the FH1 domain of mDia1 through its SH3 domain[27] (**Fig 1A**), we obtained the same results with the C-terminal portion of SPIN90, indicating that the SH3 domain of SPIN90 is not necessary for mDia1 to bind the SPIN90-Arp2/3 complex (**Fig S15A**).

To further probe the existence of a ternary complex, we performed negative staining electron microscopy experiments using mixtures of Arp2/3 with and without SPIN90 and mDia1 (Supplementary Methods). When mDia1 was added to the Arp2/3 complex, 3D reconstructions of Arp2/3 could be docked with published structures[43] with no additional electron density (**Fig 6B**). When SPIN90 was added to the Arp2/3 complex, an additional electron density was present in the region where SPIN90 has been shown to interact with Arp2/3 [44] (**Fig 6B**, **S14**). Finally, when both SPIN90 and mDia1 were included, a further electron density that could be docked with a dimer of FH2 was present close to the Arp2 and Arp3 subunits (**Fig 6B**, **S14**). These results confirm the formation of a ternary SPIN90-Arp2/3-mDia1 complex, and suggest that mDia1 may interact with the Arp2/3 complex rather than with SPIN90 in the ternary complex.

To characterize the nucleation of filaments by the ternary SPIN90-Arp2/3-mDia1 complex, we used a microfluidics assay in which we exposed a SPIN90-decorated surface sequentially to Arp2/3 followed by mDia1, before flowing in profilin-actin to enable filament nucleation and growth (**Fig. 6C-E**). We observed three populations of filaments: (*i*) slow growing filaments, (*ii*) filaments that elongated slowly and suddenly switched to rapid elongation, and (*iii*) filaments elongating rapidly from the start, which we interpreted as nucleated by the ternary complex.

The nucleation rate of population (i) was identical to that of the filaments in a region of the same microchamber which we did not expose to mDia1 (**Fig 6E**, **Fig S15C**), and to that measured in an independent experiment with no mDia1 (**Fig S11A**) indicating that population (i) corresponds to filaments nucleated by SPIN90-Arp2/3 that did not bind mDia1. The nucleation rate of population (ii) was comparable to population (i). We thus hypothesized that these slow-then-fast growing filaments were also nucleated by SPIN90-Arp2/3 and later captured an mDia1 adsorbed on the surface. Control experiments where fresh barbed ends were elongated in the same microchamber (**Fig S15B**, Supplementary Methods) indicated that such events could indeed account for a significant fraction of population (ii). The filaments in population (iii) were nucleated 5-fold faster than the filaments nucleated by SPIN90-Arp2/3 (**Fig 6E**), consistent with the notion that they are nucleated by the ternary SPIN90-Arp2/3-mDia1 complex. The aforementioned control experiment (**Fig S15B**) also confirmed that population (iii) does not result from the capture of mDia1 after nucleation. Our results thus indicate that the ternary SPIN90-Arp2/3-mDia1 complex is a much more potent nucleator than SPIN90-Arp2/3, and that the resulting filaments have SPIN90-Arp2/3 bound to their pointed end and mDia1 bound to their barbed end.

To directly observe nucleation of filaments by this ternary complex, we performed single molecule experiments using SNAP549-labeled mDia1 and Alexa647-labeled SPIN90 (50% labeled, Supplementary Methods). When mixing these proteins with Arp2/3, profilin and actin (15% Alexa488 labeled), we observed rapidly growing filaments bearing SNAP549-mDia1 at their barbed end. Even though Alexa647-SPIN90 was less active than unlabeled SPIN90, it could be observed residing at the pointed end of these rapidly growing filaments (**Fig 6F**), reminiscent of a recent report using labeled Dip1, a yeast homolog of SPIN90, in the absence of formins[23]. This observation illustrates that, as in the absence of mDia1 (**Fig S11A**), SPIN90 and Arp2/3 remain at the pointed end of filaments after nucleation (**Fig 6C-E**). Filament nucleation was challenging to observe but, colocalization of Alexa647-SPIN90 with SNAP549-mDia1 could sometimes be observed prior to the appearance of Alexa488-actin, which then separated the peaks of SPIN90 and mDia1 fluorescence, as expected since each protein occupies a different end of the growing filament (**Fig 6G**).

Together, our *in vitro* observations show that SPIN90 activates Arp2/3 to nucleate linear filaments at the expense of Arp2/3 branching, and that these filaments have an enhanced likelihood to bear mDia1 at their barbed ends thanks to (at least) two key features: the efficient recruitment of mDia1 to SPIN90-Arp2/3 nucleated filaments and the formation of a ternary complex SPIN90-Arp2/3-mDia1 that greatly enhances filament nucleation. Both mechanisms result in rapidly elongating filaments with mDia1 at their barbed ends and SPIN90-Arp2/3 at their pointed ends (**Fig 6G, 7A**).

Discussion

Using proteomics on cortex-enriched cellular fractions, we identify an NPF, SPIN90, that synergizes the action of Arp2/3 and mDia1. Cellular assays reveal a central role for SPIN90 in governing cortical actin network organization, turnover kinetics, and cell mechanics. In vitro assays show that SPIN90 controls the organization of F-actin networks by regulating the degree of branching and the fraction of rapidly growing filaments with formins at their barbed ends. SPIN90 also plays a role in tissue morphogenesis, suggesting that NPFs widely regulate F-actin network organization and cell mechanics.

The organization of F-actin networks is central to specifying their physiological function and mechanics. Understanding their homeostasis and what mediates the passage from one network organization to another is a key unresolved question in cell biology. Competition between nucleators has been proposed as a mechanism to specify structures. Indeed, the passage from the two dimensional branched network topologies found in lamellipodia to the one dimensional topologies present in filopodia appears mediated by competition between actin nucleators for G-actin monomers, regulated by profilin[45,46]. We report here that SPIN90, which thus far had only been considered as a mechanism to nucleate the mother filaments for the formation of branched networks and as a means to modulate branching density ([24,25], **Fig 4**), is actually a potent enhancer of formin mDia1. SPIN90 thereby tunes the relative contributions of Arp2/3-branching by competing with the branching reaction and co-opts formins to generate long rapidly-elongating filaments to generate a rich variety of actin filament networks (**Fig 7B**). Importantly, such transitions were observed for ratios of SPIN90 to WRC close to those present in cells (**Table S1**). Overall, our data indicate that SPIN90 regulates branching, filament growth rate and the resulting filament length, which are key parameters of the network's architecture (**Fig 7B**).

How cooperation between formins and the Arp2/3 complex occurs at the molecular level remains poorly understood. Previous work examining the lamellipodium has proposed that free barbed ends may capture FMNL2 formins following branch nucleation[18]. Our data reveal that SPIN90 allows synergistic action between mDia1 and Arp2/3 through at least two mechanisms, both resulting in

increased nucleation of fast growing actin filaments with SPIN90-Arp2/3 at their pointed ends and mDia1 at their barbed ends (**Fig 7A**).

First, mDia1 displays an enhanced affinity for the barbed ends of filaments generated by SPIN90-Arp2/3, leading to their rapid elongation. This surprising observation may either result from microstructural differences in the barbed ends induced at nucleation[13] or from recruitment of mDia1 to the pointed end by binding to SPIN90-Arp2/3 followed by diffusion of mDia1 along the filament shaft towards the barbed end, as already reported for mDia1 in a different context [47]. Note that a similar mechanism could also account for part of the slow-then-fast growing filament population observed in our nucleation experiment (**Fig 6C-E**). This population could arise from the formation of a different conformation of the ternary complex, where nucleated barbed ends elongate without mDia1, which remains associated with SPIN90-Arp2/3 at the pointed end and later diffuses along the filament to reach the barbed end. Future studies should investigate this possibility.

Second, we showed that SPIN90-Arp2/3 can form a ternary complex with mDia1 that increases filament nucleation five-fold compared to SPIN90-Arp2/3 alone. Our EM data (**Fig 6B**) and our single filament observations (**Fig 6C-E**) suggest that, following activation of Arp2/3 by SPIN90, a dimer of the FH2 domain of mDia1 binds to Arp2 and Arp3, which mimic a barbed end, to enhance nucleation and catalyze addition of monomers to the new filament. Such a "rocket launching" complex has been described for collaborative action of Adenomatous polyposis coli (APC) and mDia1[48] but not for Arp2/3 and mDia1, arguably the two most abundant actin nucleators. After elongation starts, our in vitro data indicate that mDia1 remains associated with the barbed end of the filament, whereas SPIN90-Arp2/3 remain at the pointed end (**Fig 6C-G**) (as already reported in the absence of mDia1[23]). This formation mechanism takes advantage of the efficient nucleation activity of the Arp2/3 complex and rapid filament elongation by mDia1.

We have quantified each of these different molecular mechanisms and found them to significantly enhance nucleation and elongation, individually (**Fig 5D, 6E**), and their combined action appears particularly effective at altering network organization (**Fig 4**). The total amounts of SPIN90 and other NPFs in cells can be estimated based on recent proteomics data and measurement of cellular actin concentration[31,49] (**Table S1**). While determining the concentrations of available, active proteins in the cortical region is more challenging (e.g., the WRC and mDia1 need to be activated and are likely bound to the membrane), we can estimate the relevant SPIN90 concentration to be in the 50-200 nM range (**Table S1**). Intriguingly, while these low, physiological concentrations of SPIN90 have a clear impact on network architecture in vitro, increasing SPIN90 concentration further enhances these effects without seemingly reaching saturation (**Fig 4**). This observation is reminiscent of the activation of Arp2/3 by SPIN90, which we could not saturate in our experiments (**Fig S10**), consistent with previous reports with the yeast homolog Dip1[24]. It suggests that in vitro experiments so far have not explored the full potential of SPIN90, raising the possibility that co-factors may exist in cells to favor the action of SPIN90. In addition, in cells, our electron microscopy and actin regrowth kinetics data indicate that IQGAP1 also modulates mDia1 activity (**Figs 1-2**). IQGAP1 may bind active mDia1 following release from the ternary complex (**Fig 7A**), allowing to maintain elongation activity through its C-terminal DBR domain (**Fig 1A**) and perhaps to scaffold mDia1 to the cortex through its N-terminal CHD domains.

Overall, our data show that the activity of the two main cortical actin nucleators, mDia1 and Arp2/3, is modulated by the interplay of three NPFs to finely tune cortical actin organization, kinetics, and mechanics. SPIN90 controls branching in competition with the WRC and filament length (potentially together with IQGAP1). Further work will be necessary to determine how widespread such control is in adult physiology and development, if SPIN90 also participates in the genesis of other cellular actin structures, and if similar ternary complexes exist for other formins.

References

1 Salbreux, G., Charras, G. & Paluch, E. Actin cortex mechanics and cellular morphogenesis. *Trends in Cell Biology* **22**, 536-545, doi:http://dx.doi.org/10.1016/j.tcb.2012.07.001 (2012).

2 Ramanathan, S. P. *et al.* Cdk1-dependent mitotic enrichment of cortical myosin II promotes cell rounding against confinement. *Nat Cell Biol* **17**, 148-159, doi:10.1038/ncb3098 (2015).

3 Chugh, P. *et al.* Actin cortex architecture regulates cell surface tension. *Nat Cell Biol* **19**, 689-697, doi:10.1038/ncb3525 (2017).

4 Ennomani, H. *et al.* Architecture and Connectivity Govern Actin Network Contractility. *Curr Biol* **26**, 616-626, doi:10.1016/j.cub.2015.12.069 (2016).

5 Kovar, D. R. & Pollard, T. D. Progressing actin: Formin as a processive elongation machine. *Nat Cell Biol* **6**, 1158-1159, doi:10.1038/ncb1204-1158 (2004).

6 Romero, S. *et al.* Formin is a processive motor that requires profilin to accelerate actin assembly and associated ATP hydrolysis. *Cell* **119**, 419-429, doi:10.1016/j.cell.2004.09.039 (2004).

7 Fritzsche, M., Erlenkamper, C., Moeendarbary, E., Charras, G. & Kruse, K. Actin kinetics shapes cortical network structure and mechanics. *Sci Adv* **2**, e1501337, doi:10.1126/sciadv.1501337 (2016).

8 Acharya, B. R. *et al.* Mammalian Diaphanous 1 Mediates a Pathway for E-cadherin to Stabilize Epithelial Barriers through Junctional Contractility. *Cell Rep* **18**, 2854-2867, doi:10.1016/j.celrep.2017.02.078 (2017).

9 Bovellan, M. *et al.* Cellular control of cortical actin nucleation. *Curr Biol* **24**, 1628-1635, doi:10.1016/j.cub.2014.05.069 (2014).

10 May, R. C., Caron, E., Hall, A. & Machesky, L. M. Involvement of the Arp2/3 complex in phagocytosis mediated by FcgammaR or CR3. *Nat Cell Biol* **2**, 246-248, doi:10.1038/35008673 (2000).

11 Ridley, A. J. Life at the leading edge. *Cell* **145**, 1012-1022, doi:10.1016/j.cell.2011.06.010 (2011).

12 Seth, A., Otomo, C. & Rosen, M. K. Autoinhibition regulates cellular localization and actin assembly activity of the diaphanous-related formins FRLalpha and mDia1. *J Cell Biol* **174**, 701-713, doi:10.1083/jcb.200605006 (2006).

13 Michelot, A. & Drubin, D. G. Building distinct actin filament networks in a common cytoplasm. *Curr Biol* **21**, R560-569, doi:10.1016/j.cub.2011.06.019 (2011).

14 Murrell, M., Oakes, P. W., Lenz, M. & Gardel, M. L. Forcing cells into shape: the mechanics of actomyosin contractility. *Nat Rev Mol Cell Biol* **16**, 486-498, doi:10.1038/nrm4012 (2015).

15 Okada, K. *et al.* Adenomatous polyposis coli protein nucleates actin assembly and synergizes with the formin mDia1. *J Cell Biol* **189**, 1087-1096, doi:10.1083/jcb.201001016 (2010).

16 Quinlan, M. E., Hilgert, S., Bedrossian, A., Mullins, R. D. & Kerkhoff, E. Regulatory interactions between two actin nucleators, Spire and Cappuccino. *J Cell Biol* **179**, 117-128, doi:10.1083/jcb.200706196 (2007).

17 Montaville, P. *et al.* Spire and Formin 2 synergize and antagonize in regulating actin assembly in meiosis by a ping-pong mechanism. *PLoS Biol* **12**, e1001795, doi:10.1371/journal.pbio.1001795 (2014).

18 Block, J. *et al.* FMNL2 drives actin-based protrusion and migration downstream of Cdc42. *Curr Biol* **22**, 1005-1012, doi:10.1016/j.cub.2012.03.064 (2012).

19 Campellone, K. G. & Welch, M. D. A nucleator arms race: cellular control of actin assembly. *Nat Rev Mol Cell Biol* **11**, 237-251, doi:10.1038/nrm2867 (2010).

20 Brandt, D. T. *et al.* Dia1 and IQGAP1 interact in cell migration and phagocytic cup formation. *J Cell Biol* **178**, 193-200, doi:10.1083/jcb.200612071 (2007).

21 Foroutannejad, S., Rohner, N., Reimer, M., Kwon, G. & Schober, J. M. A novel role for IQGAP1 protein in cell motility through cell retraction. *Biochem Biophys Res Commun* **448**, 39-44, doi:10.1016/j.bbrc.2014.04.038 (2014).

22 Gorman, J. A. *et al.* The cytoskeletal adaptor protein IQGAP1 regulates TCR-mediated signaling and filamentous actin dynamics. *J Immunol* **188**, 6135-6144, doi:10.4049/jimmunol.1103487 (2012).
23 Balzer, C. J., Wagner, A. R., Helgeson, L. A. & Nolen, B. J. Dip1 Co-opts Features of Branching Nucleation to Create Linear Actin Filaments that Activate WASP-Bound Arp2/3 Complex. *Curr Biol* **28**, 3886-3891 e3884, doi:10.1016/j.cub.2018.10.045 (2018).
24 Wagner, A. R., Luan, Q., Liu, S. L. & Nolen, B. J. Dip1 defines a class of Arp2/3 complex activators that function without preformed actin filaments. *Curr Biol* **23**, 1990-1998, doi:10.1016/j.cub.2013.08.029 (2013).
25 Balzer, C. J., Wagner, A. R., Helgeson, L. A. & Nolen, B. J. Single-Turnover Activation of Arp2/3 Complex by Dip1 May Balance Nucleation of Linear versus Branched Actin Filaments. *Curr Biol* **29**, 3331-3338 e3337, doi:10.1016/j.cub.2019.08.023 (2019).
26 Eisenmann, K. M. *et al.* Dia-interacting protein modulates formin-mediated actin assembly at the cell cortex. *Curr Biol* **17**, 579-591, doi:10.1016/j.cub.2007.03.024 (2007).
27 Satoh, S. & Tominaga, T. mDia-interacting protein acts downstream of Rho-mDia and modifies Src activation and stress fiber formation. *J Biol Chem* **276**, 39290-39294, doi:10.1074/jbc.M107026200 (2001).
28 Higashi, T. *et al.* Flightless-I (Fli-I) regulates the actin assembly activity of diaphanous-related formins (DRFs) Daam1 and mDia1 in cooperation with active Rho GTPase. *J Biol Chem* **285**, 16231-16238, doi:10.1074/jbc.M109.079236 (2010).
29 Dephoure, N. *et al.* A quantitative atlas of mitotic phosphorylation. *Proc Natl Acad Sci U S A* **105**, 10762-10767, doi:10.1073/pnas.0805139105 (2008).
30 Olsen, J. V. *et al.* Quantitative phosphoproteomics reveals widespread full phosphorylation site occupancy during mitosis. *Sci Signal* **3**, ra3, doi:10.1126/scisignal.2000475 (2010).
31 Bekker-Jensen, D. B. *et al.* An Optimized Shotgun Strategy for the Rapid Generation of Comprehensive Human Proteomes. *Cell Syst* **4**, 587-599 e584, doi:10.1016/j.cels.2017.05.009 (2017).
32 Charras, G. T., Hu, C. K., Coughlin, M. & Mitchison, T. J. Reassembly of contractile actin cortex in cell blebs. *J Cell Biol* **175**, 477-490 (2006).
33 Clark, A. G., Dierkes, K. & Paluch, E. K. Monitoring actin cortex thickness in live cells. *Biophys J* **105**, 570-580, doi:10.1016/j.bpj.2013.05.057 (2013).
34 Biro, M. *et al.* Cell cortex composition and homeostasis resolved by integrating proteomics and quantitative imaging. *Cytoskeleton (Hoboken)* **70**, 741-754, doi:10.1002/cm.21142 (2013).
35 Vargas-Pinto, R., Gong, H., Vahabikashi, A. & Johnson, M. The effect of the endothelial cell cortex on atomic force microscopy measurements. *Biophys J* **105**, 300-309, doi:10.1016/j.bpj.2013.05.034 (2013).
36 Bergert, M., Chandradoss, S. D., Desai, R. A. & Paluch, E. Cell mechanics control rapid transitions between blebs and lamellipodia during migration. *Proc Natl Acad Sci U S A* **109**, 14434-14439, doi:10.1073/pnas.1207968109 (2012).
37 Toyoda, Y. *et al.* Genome-scale single-cell mechanical phenotyping reveals disease-related genes involved in mitotic rounding. *Nat Commun* **8**, 1266, doi:10.1038/s41467-017-01147-6 (2017).
38 Sullivan-Brown, J. L. *et al.* Identifying Regulators of Morphogenesis Common to Vertebrate Neural Tube Closure and Caenorhabditis elegans Gastrulation. *Genetics* **202**, 123-139, doi:10.1534/genetics.115.183137 (2016).
39 Sokol, S. Y., Li, Z. & Sacks, D. B. The effect of IQGAP1 on Xenopus embryonic ectoderm requires Cdc42. *J Biol Chem* **276**, 48425-48430, doi:10.1074/jbc.M107975200 (2001).
40 Higashi, T., Stephenson, R. E. & Miller, A. L. Comprehensive analysis of formin localization in Xenopus epithelial cells. *Mol Biol Cell* **30**, 82-95, doi:10.1091/mbc.E18-02-0133 (2019).

41 Jones, E. A. & Woodland, H. R. Development of the ectoderm in Xenopus: tissue specification and the role of cell association and division. *Cell* **44**, 345-355 (1986).
42 Cao, L. *et al.* Modulation of formin processivity by profilin and mechanical tension. *Elife* **7**, doi:10.7554/eLife.34176 (2018).
43 Jurgenson, C. T. & Pollard, T. D. Crystals of the Arp2/3 complex in two new space groups with structural information about actin-related protein 2 and potential WASP binding sites. *Acta Crystallogr F Struct Biol Commun* **71**, 1161-1168, doi:10.1107/S2053230X15013515 (2015).
44 Luan, Q., Liu, S. L., Helgeson, L. A. & Nolen, B. J. Structure of the nucleation-promoting factor SPIN90 bound to the actin filament nucleator Arp2/3 complex. *EMBO J*, doi:10.15252/embj.2018100005 (2018).
45 Rotty, J. D. & Bear, J. E. Competition and collaboration between different actin assembly pathways allows for homeostatic control of the actin cytoskeleton. *Bioarchitecture* **5**, 27-34, doi:10.1080/19490992.2015.1090670 (2014).
46 Suarez, C. *et al.* Profilin regulates F-actin network homeostasis by favoring formin over Arp2/3 complex. *Dev Cell* **32**, 43-53, doi:10.1016/j.devcel.2014.10.027 (2015).
47 Bombardier, J. P. *et al.* Single-molecule visualization of a formin-capping protein 'decision complex' at the actin filament barbed end. *Nat Commun* **6**, 8707, doi:10.1038/ncomms9707 (2015).
48 Breitsprecher, D. *et al.* Rocket launcher mechanism of collaborative actin assembly defined by single-molecule imaging. *Science* **336**, 1164-1168, doi:10.1126/science.1218062 (2012).
49 Funk, J. *et al.* Profilin and formin constitute a pacemaker system for robust actin filament growth. *Elife* **8**, doi:10.7554/eLife.50963 (2019).

Acknowledgements
This article is dedicated to the memory of Art Alberts who passed away during completion of this study. The authors thank present and past members of the Charras, Romet/Jegou, Paluch, and Roux labs for support and discussion over the course of the project. AY, MV, PC, and MB were supported by HFSP Young Investigator grants to GC, EP, GR, and PR (RGY66/2013). PC and EP acknowledge the support of the Medical Research Council UK (MRC programme award MC_UU_12018/5). EF was funded by a European Research Council consolidator grant to GC (CoG-647186). EB was supported by BBSRC grant (BB/R00627) to GC and RM. LC was supported by a grant from Fondation pour la Recherche Médicale to GRL. JM was supported by a grant from the Agence Nationale de la Recherche to AB and GRL (ANR grant Conformin). AJ was supported by a European Research Council starting grant (StG-679116). AFM equipment was funded by a BBSRC Alert16 grant to GC (BB/R000042). AM and GL were supported by an Operating grant from the Canadian Institute of Health Research to P.P.R. (MOP‑142374). PPR is supported by a FRQS Senior investigator career award. The authors also wish to thank Henry Higgs, Robert Grosse, Brad Nolen, David Sacks, Robert Tombes, and Orion Weiner for reagents.

Author contributions
GC, GRL, AJ, AY, LC, and MV designed the experiments. AY carried out all electron microscopy on cells, long term microscopy, and bleb size characterization. MV carried out all laser ablation, AFM and fluorescence quantification experiments. LC, GRL, AJ carried out in vitro experiments. PC did all measurements of cortex thickness and F-actin density. MS designed the software for analysis of SEM images. GL, AM, and PPR performed all proteomic and qPCR experiments and analyzed data. AY and EF did all Western blots. GC generated live imaging constructs and carried out immunostainings. JM and AB carried out the molecular-scale electron microscopy and generated the complex structures. MB contributed live imaging constructs and some imaging experiments. AA provided plasmid constructs. EB and RM contributed Xenopus experiments. EP provided conceptual advice. GC and GRL wrote the manuscript. All authors discussed the results and the manuscript.

Figures

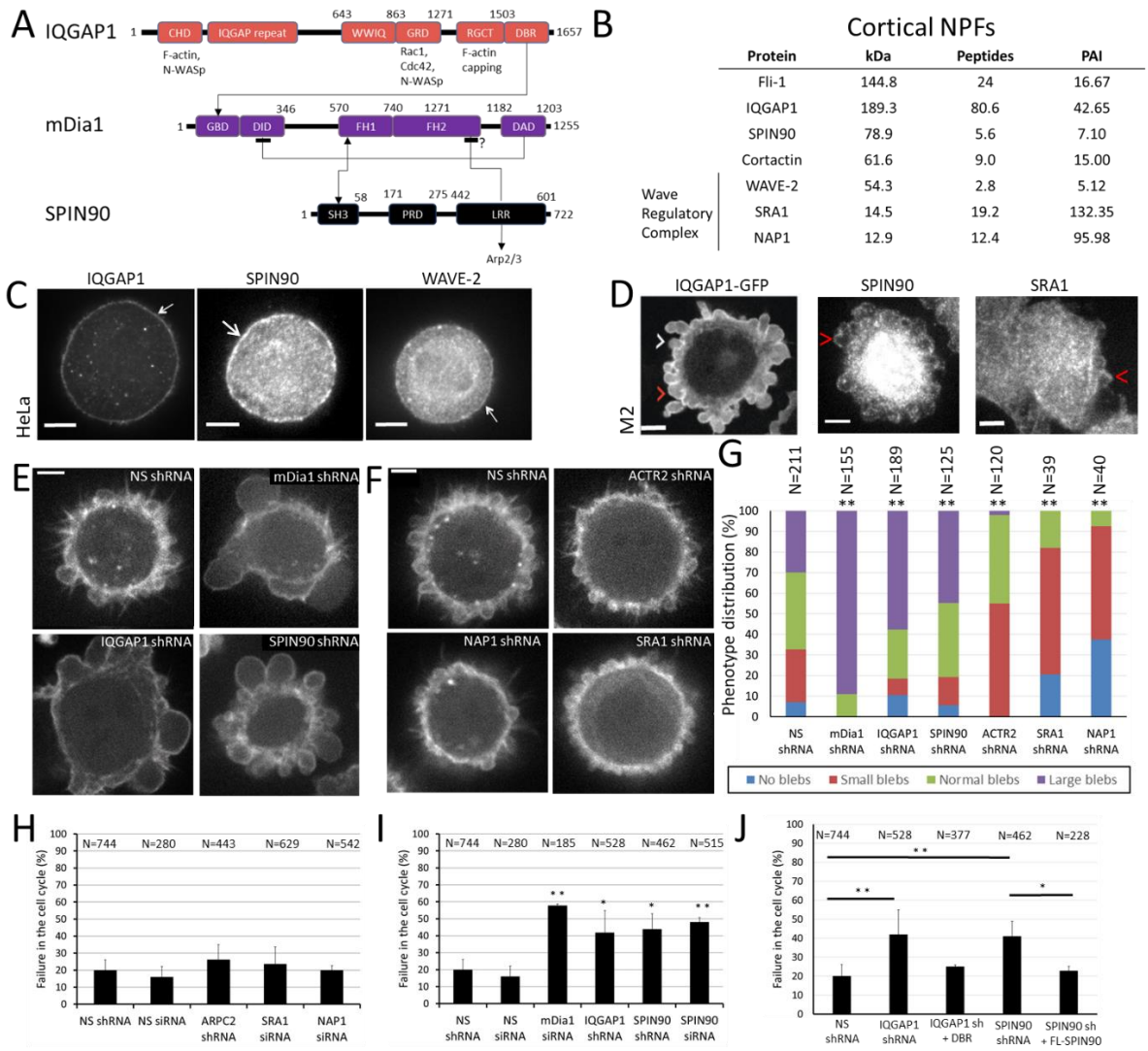

Figure 1: Several Nucleation Promoting Factors are present in the actin cortex and their depletion leads to changes in cell morphology and cell death. A. Domain structure of IQGAP1, mDia1, and SPIN90. Numbers refer to amino-acid position from the N terminus. Known protein interactors are displayed under each domain. Known positive and inhibitory interactions between IQGAP1, mDia1, and SPIN90 are indicated. Direct inhibitory interaction between the LRR domain of SPIN90 and the FH2 domain has been demonstrated for mDia2 but not for mDia1[26]. **B.** NPFs detected in the detergent-insoluble fraction of blebs separated from M2 blebbing melanoma cells. Subunits of the same complex are displayed together. Protein isoforms are grouped together. Detected peptide numbers are averaged over three separate experiments. Protein abundance index (PAI) was calculated based on spectral counts (see **SI**). **C.** Immunofluorescence image of the localization of NPFs in metaphase HeLa cells. Arrows indicate cortical localization. Scale bars=5µm. **D.** Localization of NPFs in M2 blebbing melanoma cells. IQGAP1 localization was obtained through transient transfection with IQGAP1-GFP. The SRA1 subunit of the WAVE complex and SPIN90 were detected by immunofluorescence. White arrowheads indicate expanding blebs and red arrowheads retracting ones. Scale bars=5µm. **E.** Live confocal microscopy images of M2 blebbing melanoma cells stably expressing LifeAct-Ruby and stably transduced with shRNA targeting mDia1, IQGAP1, and SPIN90 as well as Non-Silencing shRNA (NS shRNA). **F.** Live confocal microscopy images of M2 blebbing melanoma cells stably expressing LifeAct-Ruby and stably transduced with shRNA targeting ACTR2 (the Arp2 subunit of the Arp2/3 complex),

NAP1, and SRA1 as well as Non-Silencing shRNA. **(E-F).** Scale bars=5 µm. **G.** Distribution of bleb sizes in M2 melanoma cells stably expressing Non-Silencing shRNA, mDia1 shRNA, ACTR2 shRNA, IQGAP1 shRNA, SPIN90 shRNA, SRA1 shRNA, and NAP1 shRNA. The number of cells examined in each experiment is indicated above each column. When compared to cells stably expressing Non-Silencing shRNA, all depleted cell lines showed significantly different bleb distributions (**, $p<0.01$). Statistical analysis and raw data are reported in **Table S2**. Comparison to Non-Silencing shRNA with Chi-squared test: mDia1: $p=3\ 10^{-56}$; IQGAP1: $p=3\ 10^{-18}$; SPIN90: $p=6\ 10^{-4}$; ACTR2: $p=2\ 10^{-17}$; SRA1: $p=1\ 10^{-9}$; NAP1: $p=4\ 10^{-18}$ **(H-J).** The percentage of HeLa cells failing to progress through the cell cycle was determined for different depletions using long-term time-lapse microscopy. The number of cells examined in each experiment is indicated above each column. **H.** Cells transfected with ARPC2 shRNA, SRA1 siRNA, and NAP1 siRNA progressed normally through the cell cycle. Statistical comparison to Non-Silencing with Welch's t-test: ARPC2: $p=0.24$; SRA1: $p=0.14$; NAP1: $p=0.15$. **I.** When compared to cells transfected with Non-Silencing siRNA or shRNA, cells transfected with mDia1 siRNA, IQGAP1 shRNA, and SPIN90 si/shRNA showed significantly reduced rates of successful cell cycle progression (*, $p<0.05$; **, $p<0.01$). Statistical comparison to Non-Silencing with Welch's t-test: mDia1: $p=9\ 10^{-5}$; IQGAP1: $p=0.026$; SPIN90 siRNA: $p=1\ 10^{-4}$; SPIN90 shRNA: $p=0.01$. **J.** Failure to progress through the cell cycle for cells expressing IQGAP1 shRNA could be rescued by transfection with the DBR domain of mouse IQGAP1 tagged with EBFP2. Failure to progress through the cell cycle for cells expressing SPIN90 shRNA could be rescued by transfection with full-length mouse SPIN90 tagged with EBFP2. Statistical comparison to Non-Silencing with Welch's t-test: IQGAP1+DBR: $p=0.33$; SPIN90 shRNA + FL: $p=0.7$. **(G-J)** Experiments were repeated at least three times on independent days.

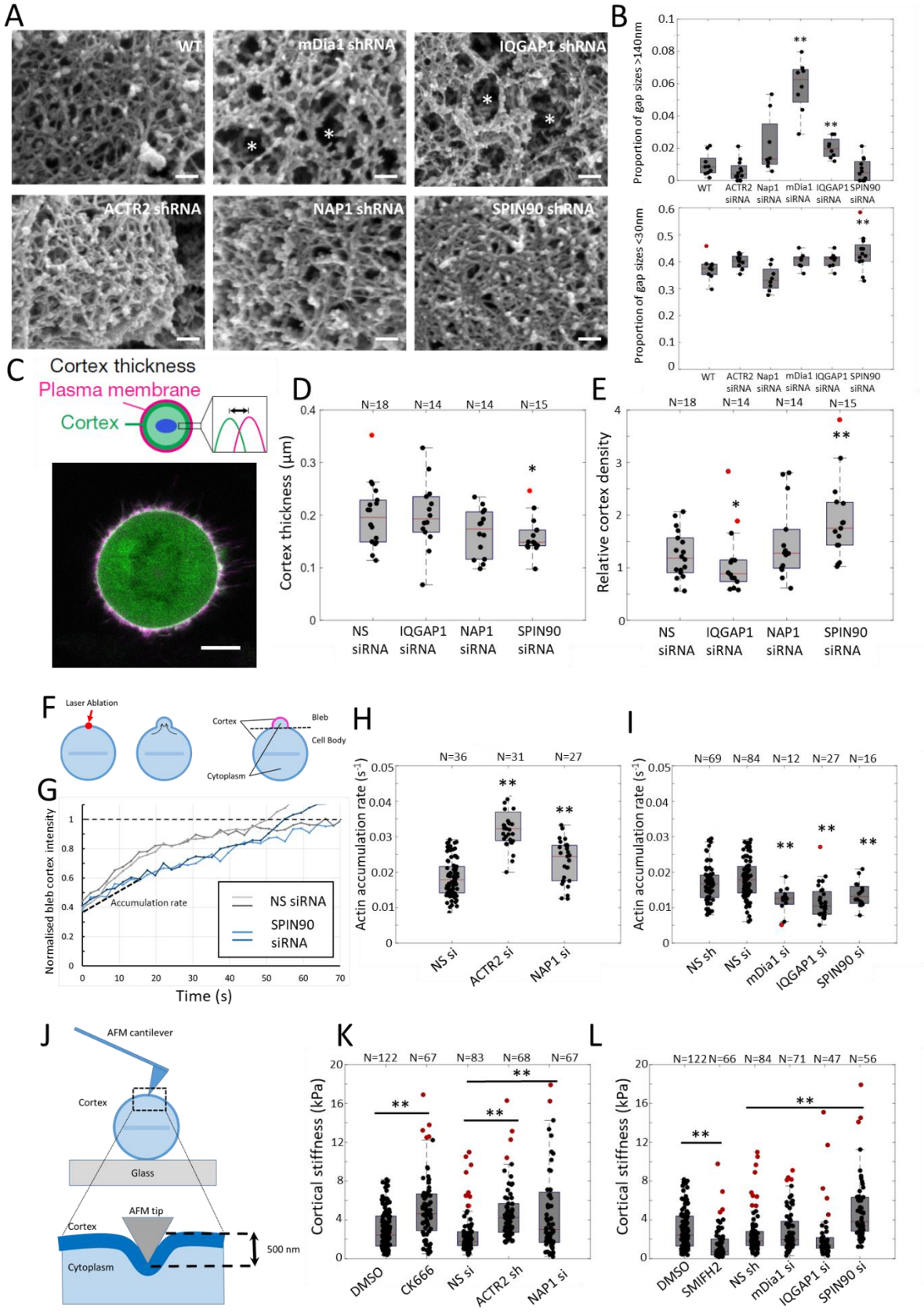
A
WT
mDia1 shRNA
IQGAP1 shRNA
ACTR2 shRNA
NAP1 shRNA
SPIN90 shRNA
B
Proportion of gap sizes >140nm
Proportion of gap sizes <30nm
WT
ACTR2 siRNA
Nap1 siRNA
mDia1 siRNA
IQGAP1 siRNA
SPIN90 siRNA
C
Cortex thickness
Plasma membrane
Cortex
D
Cortex thickness (µm)
N=18 N=14 N=14 N=15
NS siRNA
IQGAP1 siRNA
NAP1 siRNA
SPIN90 siRNA
E
Relative cortex density
F
Laser Ablation
Cortex
Bleb
Cell Body
Cytoplasm
G
Normalised bleb cortex intensity
Accumulation rate
NS siRNA
SPIN90 siRNA
Time (s)
H
Actin accumulation rate (s⁻¹)
N=36 N=31 N=27
NS si
ACTR2 si
NAP1 si
I
N=69 N=84 N=12 N=27 N=16
NS sh
NS si
mDia1 si
IQGAP1 si
SPIN90 si
J
AFM cantilever
Cortex
Glass
AFM tip
Cytoplasm
500 nm
K
Cortical stiffness (kPa)
N=122 N=67 N=83 N=68 N=67
DMSO
CK666
NS si
ACTR2 sh
NAP1 si
L
N=122 N=66 N=84 N=71 N=47 N=56
DMSO
SMIFH2
NS sh
mDia1 si
IQGAP1 si
SPIN90 si

Figure 2: SPIN90 controls cortex molecular-scale organization, kinetics, and mechanics. A. Representative scanning electron micrographs of the actin cortex at the surface of a bleb in detergent-extracted M2 cells stably expressing non-silencing shRNA or shRNA targeting nucleators or NPFs. Asterisks highlight large gaps in the cortex. Scale bars = 100 nm. **B.** Frequency distribution of gap diameters within the cortical mesh of blebs in M2 cells. Data points showing a significant change in proportion compared to WT are indicated by asterisks (**p≤0.01). Comparison to WT with Wilcoxon's rank test for small mesh sizes (<30nm): Arp2: p=0.03; Nap1: p=0.12; mDia1: p=0.08; IQGAP1: p=0.04; SPIN90: p=0.01. For large mesh sizes (>140nm): Arp2: p=0.24; Nap1: p=0.09; mDia1: p=0.01; IQGAP1: p=0.01; SPIN90: p=0.81. The full distributions are presented in **Fig S5**. **C.** Top: Schematic representation of the measurement: cortex thickness and density are extracted from the fluorescence profiles of mCherry-CAAX (plasma membrane) and GFP-actin (cortex) in prometaphase HeLa cells[33]. Bottom: Representative confocal image of a prometaphase HeLa cell expressing GFP-actin (green) and mCherry-CAAX (magenta). Scale bar=10 µm. **D.** Cortex thickness for prometaphase HeLa cells transfected with non-silencing siRNA or siRNA targeting IQGAP1, NAP1, SPIN90. **E.** Cortex density for prometaphase HeLa cells transfected with non-silencing siRNA or siRNA targeting IQGAP1, NAP1, SPIN90. **D-E** *p<0.05 and **p<0.01 compared to the appropriate control with Welch's t-test. Cortex thickness: IQGAP1: p=0.59; Nap1: p=0.2; SPIN90: p=0.02. Cortex density: IQGAP1: p=0.03; Nap1: p=0.26; SPIN90: p=0.007. **F.** Single blebs are induced in metaphase HeLa cells by laser ablation of the cortex (red arrow)[34]. Right: automated image analysis is used to segment the cell into cytoplasm, cell body cortex, and bleb cortex and allows for precise measurement of the evolution of fluorescence intensity in these regions over time (**Fig S7A-C**). **G.** Representative actin regrowth curves as a function of time in blebs induced by laser ablation in a metaphase HeLa cells expressing LifeAct-Ruby and Non-silencing siRNA (grey) or SPIN90 siRNA (blue). The mean actin fluorescence intensity at the bleb cortex was normalized to the mean intensity in the cell body cortex (dashed horizontal line). Initial regrowth rates after ablation are linear with time (initial accumulation rate, dashed line). t = 0 s, ablation onset. **H-I.** Actin cortex accumulation rate in cells transfected with non-silencing siRNA/shRNA (NS si/ Ns sh) or siRNA/shRNA targeting nucleators and NPFs. Statistical comparison to the appropriate control using Student's t-test: ACTR2: p=9 10^{-20}; Nap1: p=0.002; mDia1: p=0.001; IQGAP1: p=2 10^{-5}; SPIN90: p=0.001. **J.** Principle of Atomic Force Microscopy cortex stiffness measurement. The pyramidal AFM tip indents the cell cortex (dark blue) to a depth of 500nm. As the cortex is 200nm thick on average (**D**), this signifies that cortex mechanics are the main contributor to stiffness. **K.** Cortical stiffness for control cells (DMSO, NS siRNA) and cells treated with the Arp3 inhibitor CK666 or expressing si/shRNAs targeting NAP1 and ACTR2. Controls are presented in **Fig S7D**. **L.** Cortical stiffness for control cells (DMSO, NS shRNA) and cells treated with the broad spectrum formin inhibitor SMIFH2 or expressing si/shRNAs targeting mDia1, IQGAP1, and SPIN90. Statistical comparison to the appropriate control using Student's t-test: ACTR2: p=2 10^{-18}; Nap1: p=2 10^{-10}; CK666: 2 10^{-6}; mDia1: p=0.06; IQGAP1: p=0.03; SPIN90: p=0.0002; SMIFH2: p=2 10^{-11}. **p < 0.01 compared to the appropriate control. (**B**, **D-E**, **H-I**, **K-L**) Data are plotted as box-whisker plots. Whiskers indicate minimum and maximum values. The number of cells examined is indicated above each box. Statistical outliers are indicated by red dots.

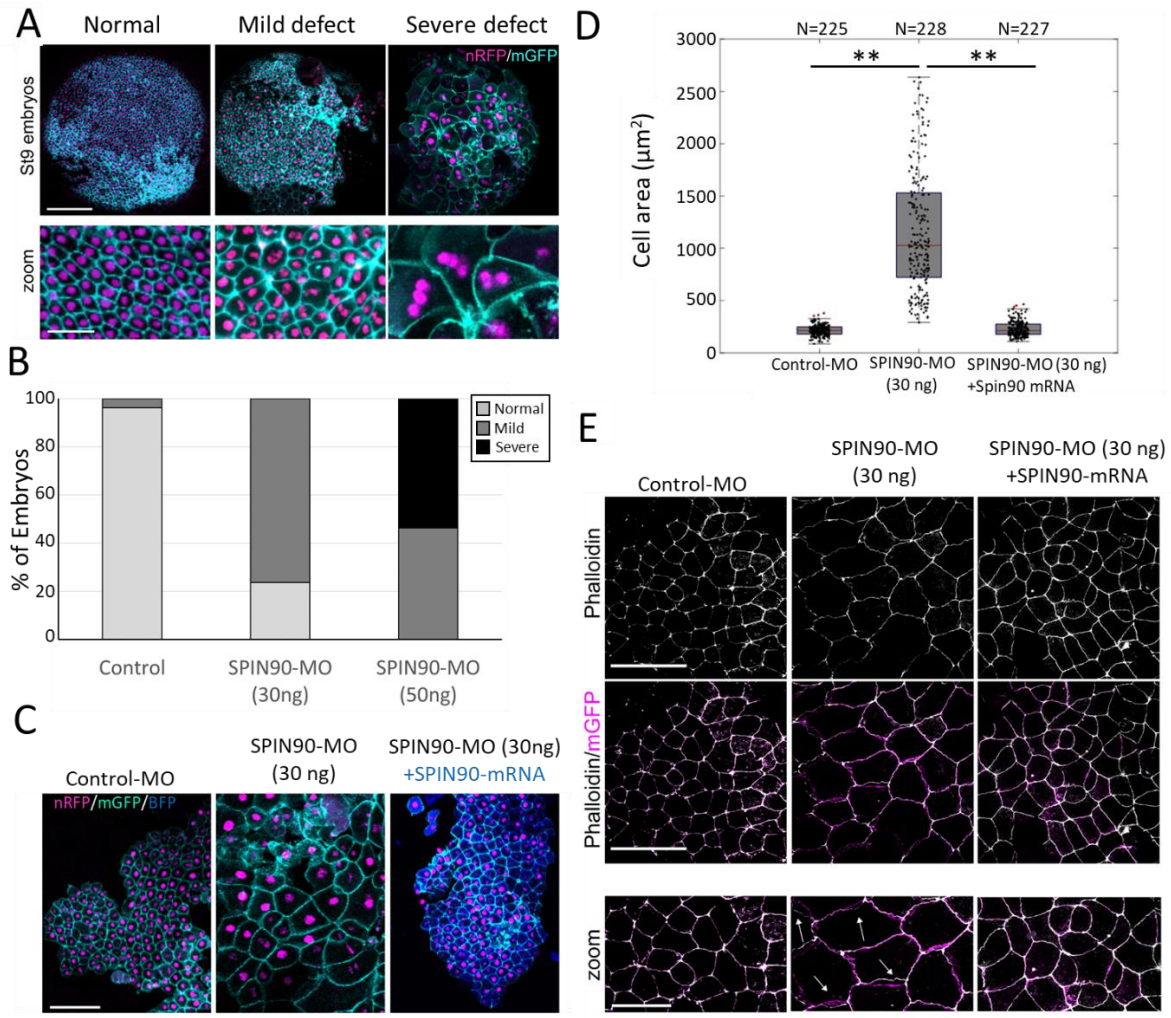

Figure 3. SPIN90 is necessary for correct development of *Xenopus* blastulae. A. Stage 9 *Xenopus* embryos (St9) were injected with Control-MO or SPIN90-MO along with nuclear targeted RFP (nRFP) and membrane targeted GFP (mGFP). Images are representative examples of normal ectoderm (left) and ectoderm with mild (middle) or severe (right) defects in cell numbers and cell size. Scale bars: top row: 150 µm; bottom row: 50 µm. **B.** Quantification of the proportion of embryos presenting normal ectoderm (light grey) and mild (dark grey) or severe (black) epidermis defects for different morpholino injections. The proportions are computed from an average of 4 different experiments examining 20 embryos each. Western blots confirming knock down are presented in **Fig S9**. **C.** Stage 9 *Xenopus* embryos (St9) co-injected with: Control-MO (30ng), SPIN90-MO (30ng), or SPIN90-MO (30ng) plus full-length mouse SPIN90-BFP, along with nuclear targeted RFP and membrane targeted GFP. The effect of SPIN90-MO was rescued by mouse SPIN90-BFP mRNA. The efficiency of the rescue was 70% with just 10% of the embryos displaying morphant phenotype, compared to ~80% displayed by SPIN90-MO treated embryos. Images are representative examples of at least 3 independent experiments. Scale bar: 100 µm. **D.** Cell area for stage 9 *Xenopus* embryos injected with Control-MO (30ng), SPIN90-MO (30ng), or SPIN90 (30ng) + mouse SPIN90 mRNA. Data are plotted as box-whisker plots. Whiskers indicate minimum and maximum values. The number of cells examined is indicated above each box. Statistical outliers are indicated by red dots. Statistical comparison with Welch's t-test: Control-MO vs SPIN90-MO: $p=3\ 10^{-131}$; SPIN90-MO vs rescue: $p=5\ 10^{-122}$; Control-MO vs rescue: p=0.20. $^{**}p < 0.01$ compared to the appropriate control. **E.** Stage 9 *Xenopus* embryos (St9) co-injected with Control-MO,

SPIN90-MO, or SPIN90-MO plus full-length mouse SPIN90-BFP mRNA, along with membrane targeted GFP. Top panels display phalloidin staining (white), central panels show the overlap with membrane targeted GFP (magenta), and lower panels show a zoom of the middle panels. In some SPIN90-MO treated cells, actin is no longer colocalized with cell membranes, white arrows. Scale bars: Top and middle panels: 100 µm. Bottom panel: 50 µm. Images are representative examples of at least 3 independent experiments.

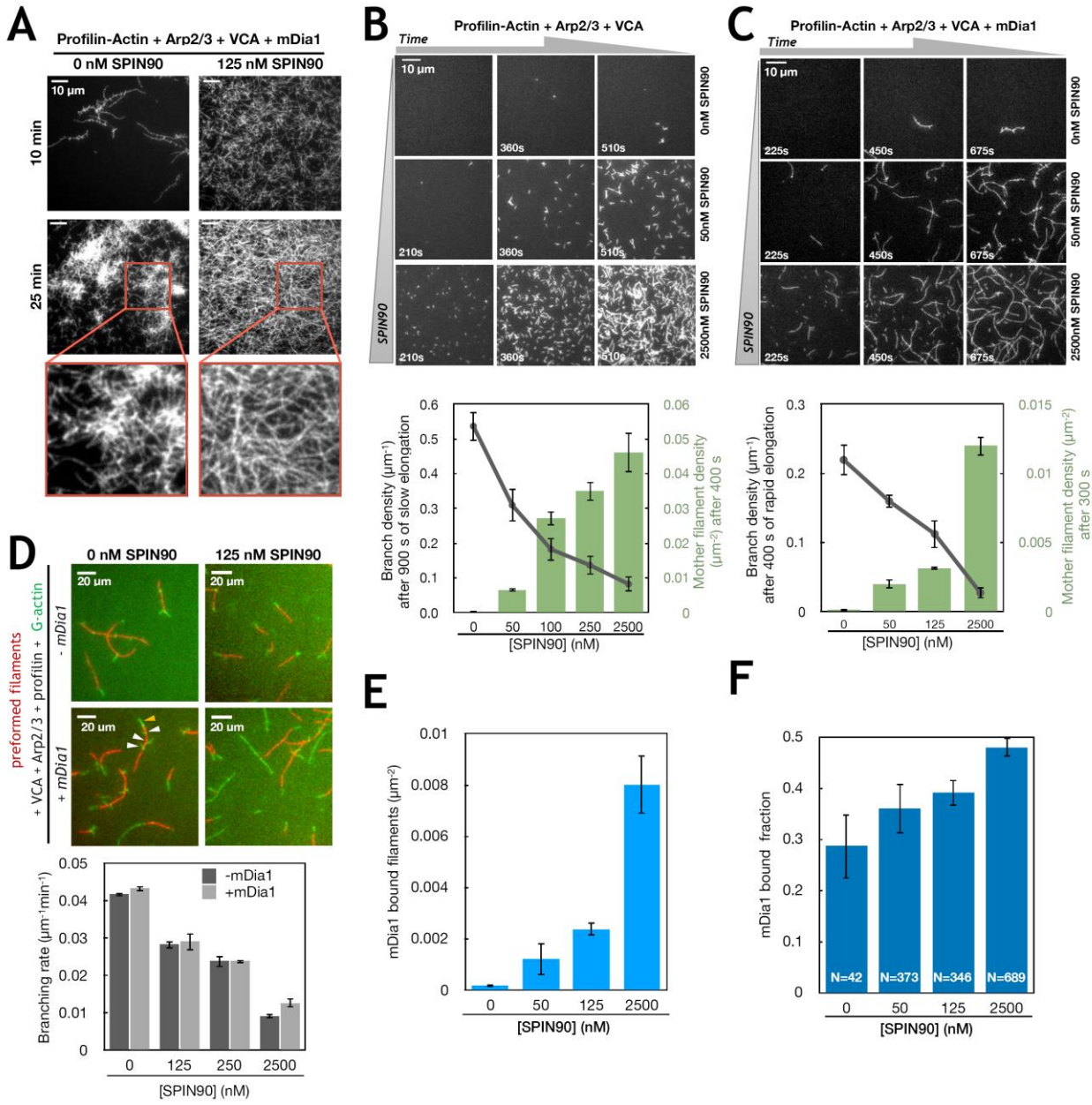

Figure 4. SPIN90 activates Arp2/3 to nucleate mDia1-elongated filaments. A. TIRF images of 0.5µM actin (15% Alexa488 labeled) polymerizing in the presence of 0.5 µM profilin, 25 nM Arp2/3 complex, 50 nM VCA, 0.2 nM mDia1, with (right) and without (left) 125 nM SPIN90. **B-C.** TIRF images of the same protein solution as in A, without mDia1 (**B**) and with 0.4 nM mDia1 (**C**), and with various concentrations of SPIN90 (indicated on the right side of each row). Plots: nucleation (green bars) is quantified by counting the number of mother filaments per surface area after 400 seconds (**B**) or 300 seconds (**C**), and averaging over 3 different fields of view (± std. dev.). The branch density (gray points) is quantified as the average number of branches per micrometer of mother filament (± std. error, n=20 mother filaments for each condition, except n=10 for 0 nM SPIN90 in **C**). Branches were counted after mother filaments had elongated for 900 s, typically becoming 5.5µm long (**B**) or after mother filaments had elongated with mDia1 for 400s, typically becoming 18µm long (**C**). **D.** TIRF microscopy images of preformed actin filaments (15% Alexa568-labeled, red) mixed with the same protein solution as in **A**, with or without 0.2 nM mDia1, with or without 125 nM SPIN90. Plot: the branching rate is determined from the number of branches appearing on the preformed mother filaments over time (**Fig. S12**), as a function of SPIN90 concentration, in the absence (dark gray bars) or presence (light gray bars) of

0.2nM mDia1. **E.** Density of rapidly growing filament barbed ends (i.e. bearing a formin), observed after 400s in the experiment shown in (**C**). **F.** Fraction of rapidly growing barbed ends (i.e. bearing a formin), observed after 400s in the experiment shown in (**E**). Error bars represent 95% confidence intervals. The number of filaments is indicated below each bar. (**D-F**) Measurements were gathered from at least two independent experiments.

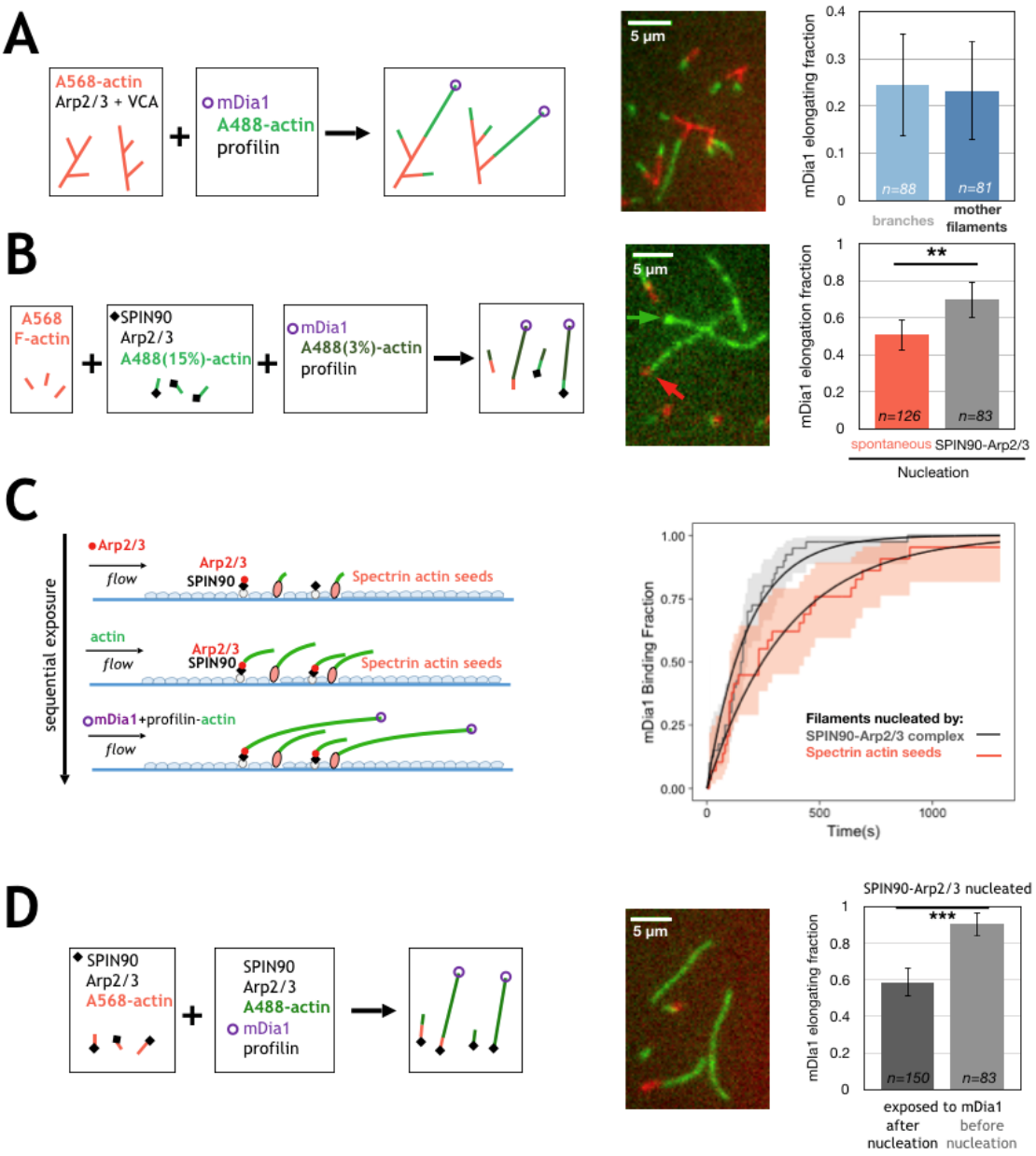

Figure 5. mDia1 preferentially binds to filaments nucleated by SPIN90-Arp2/3. A. Comparison of the affinity of mDia1 for mother filaments versus branches. Preformed branched actin filaments (15% Alexa568 labeled) were mixed with 0.5 µM G-actin (15% Alexa488-labeled), 0.5 µM profilin, 0.4nM mDia1, before being introduced into a passivated open chamber. The TIRF microscopy image shows Alexa568 in red and Alexa488 in green. Plot: fraction of rapidly growing barbed ends (i.e. bearing a formin) observed after 90s, within the population of mother filaments (dark blue bar) and branches (light blue bar). Comparison with Pearson's chi square test: p=0.88. **B.** Comparison of the affinity of mDia1 for spontaneously nucleated versus SPIN90-Arp2/3-nucleated filaments. Spontaneously nucleated actin filaments (15% Alexa568-labeled) were mixed with SPIN90-Arp2/3-nucleated actin filaments (15% Alexa488-labeled) and with 0.2nM mDia1, 0.5 µM profilin and 0.5 µM G-actin (3% Alexa488-labeled). TIRF microscopy image: filaments growing from spontaneously assembled seeds (red arrow) or from SPIN90-Arp2/3-nucleated seeds (green arrow) are identified by the fluorescence at their pointed end. Plot: fraction of rapidly growing barbed ends observed after 300s, within each population. Comparison with a Pearson's chi square test: p=0.009. **C.** Sketch of the microfluidics

experiment performed to monitor the binding of mDia1 to the barbed ends of different filament types: filaments were nucleated by surface-anchored spectrin-actin seeds or SPIN90-Arp2/3 complexes, and identified as such (Supplementary Methods and **Fig S13C**) before flowing in a solution containing 0.5 µM G-actin (15% Alexa488 labeled), 3.5 µM profilin and 0.4 nM mDia1. The binding of mDia1 was detected by the acceleration of filament elongation. Plot: measured mDia1-elongating filament fractions versus time and exponential fits (solid black lines), for the population of filaments nucleated by spectrin-actin seeds (pink, n=39 filaments, $k_{on}=2.8x10^{-3} \pm 1.1x10^{-5}$ s^{-1}) and those nucleated by SPIN90-Arp2/3 (gray, n=40 filaments, $k_{on}=5.5x10^{-3} \pm 3.5x10^{-5}$ s^{-1}). Comparison with weighted log-rank test: p=0.01. Shaded regions show 95% confidence intervals. **D.** Comparison of the fraction of mDia1-bearing barbed ends depending on filament nucleation history. SPIN90-Arp2/3-nucleated actin filaments (15% Alexa568 labeled) were mixed with 0.5 µM G-actin (15% Alexa488 labeled), 0.5 µM profilin, 25 nM Arp2/3, 250 nM SPIN90 and 0.2 nM mDia1. TIRF microscopy image: filaments nucleated before mixing (i.e. exposed to mDia1 after their nucleation by SPIN90-Arp2/3) are identified thanks to their Alexa568 (red) pointed end region. Plot: fraction of rapidly growing barbed ends observed after 300s, within each population. Comparison with a Pearson's chi square test: $p=9x10^{-7}$. (**A,B,D**) Error bars represent 95% confidence intervals. **p<0.01 and ***p<0.001, Pearson's chi-squared test.

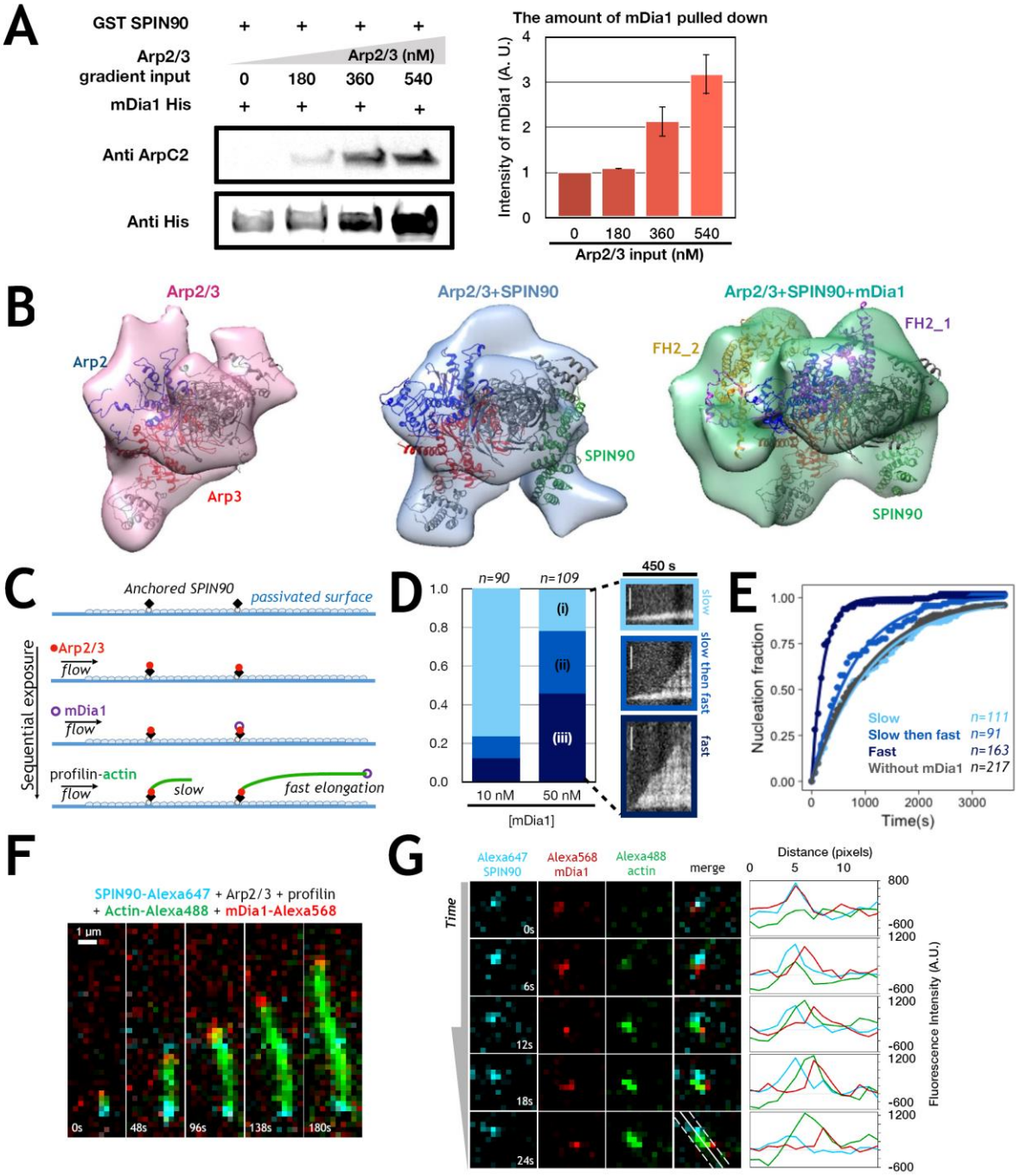

Figure 6. mDia1 forms a ternary complex with SPIN90-Arp2/3 to generate fast-elongating filaments. **A.** mDia1 is dose-dependently eluted with Arp2/3 bound to SPIN90 decorated beads. Left: Anti-His and Anti-ArpC2 western blots of GST pull down assay. GST beads were incubated with 12 µM GST-SPIN90 and with the indicated amounts of Arp2/3. The beads were washed and incubated with 750 nM mDia1. Right: quantification of pulled-down mDia1, normalized to GST-SPIN90 without Arp2/3 (mean ± SEM, n=3 independent experiments). **B.** 3D structures of protein complexes reconstructed from EM negative stains. Reconstructions obtained from Arp2/3 incubated with mDia1 (left), Arp2/3 with SPIN90 (middle) or Arp2/3 with SPIN90 and mDia1 together (right). The EM densities are fitted using UCSF Chimera with crystal structures of Arp2/3 (PDB : 4xf2) (left) or Arp2/3-SPIN90 complex (PDB : 6dec) (middle), or an atomic model made of a dimer of the FH2 domain of mDia1 (PDB : 1y64)

bound to the Arp2/3-SPIN90 complex (PDB : 6dec) (right). Each 3D reconstruction was obtained at 27Å resolution. Further orientations are displayed in **Fig S14**. **C.** Sketch of a microfluidics experiment where a SPIN90-decorated surface is sequentially exposed to Arp2/3 then mDia1, before flowing in profilin-actin. Filaments are then observed with their pointed ends attached to the surface and their barbed ends growing either slowly (bare barbed ends) or rapidly (mDia1-bearing barbed ends). **D**. Proportion of filaments elongating slow (i, light blue), slow-then-fast (ii, blue) and fast (iii, dark blue) for different mDia1 concentrations. Right: kymographs showing representative examples of each behavior. The SPIN90-decorated surface was exposed to 40 nM Arp2/3 for 120s, followed by 10 or 50 nM mDia1 for 30s, then buffer was flowed in for 120s, and finally filaments were observed in the presence of 0.5 µM actin and 0.5 µM profilin. **E.** Nucleation of the three filament populations observed in (**D**), with 50 nM mDia1: fast growing (iii, dark blue), slow-then-fast (ii, blue) and slow (i, light blue). These were compared to the nucleation of filaments in a region of the chamber not exposed to mDia1 (gray). Lines are exponential fits, yielding nucleation rates of $8.8x10^{-4}$ s^{-1} for population (i), $1.2x10^{-3}$ s^{-1} for population (ii) ($p=0.1$, log-rank test) and $4.6x10^{-3}$ s^{-1} for population (iii) ($p=2x10^{-16}$, log-rank test). (**C-E**) Data from at least two independent experiments. **F.** TIRF microscopy image sequence of an elongating filament in a solution of 0.4 µM actin (15% Alexa488 labeled, green), 0.6 µM profilin, 2 nM SPIN90-Alexa647 (cyan), 120 nM Arp2/3 and 1 nM mDia1-SNAP549 (red). **G.** TIRF microscopy image sequence of a filament nucleated from SPIN90-Alexa647 (cyan), Arp2/3 and mDia1-SNAP549 (red). Same conditions as in (**F**). All the intensity plots shown on the right were taken along the white solid line shown in the bottom right image, over the 3-pixel width indicated by the dashed lines.

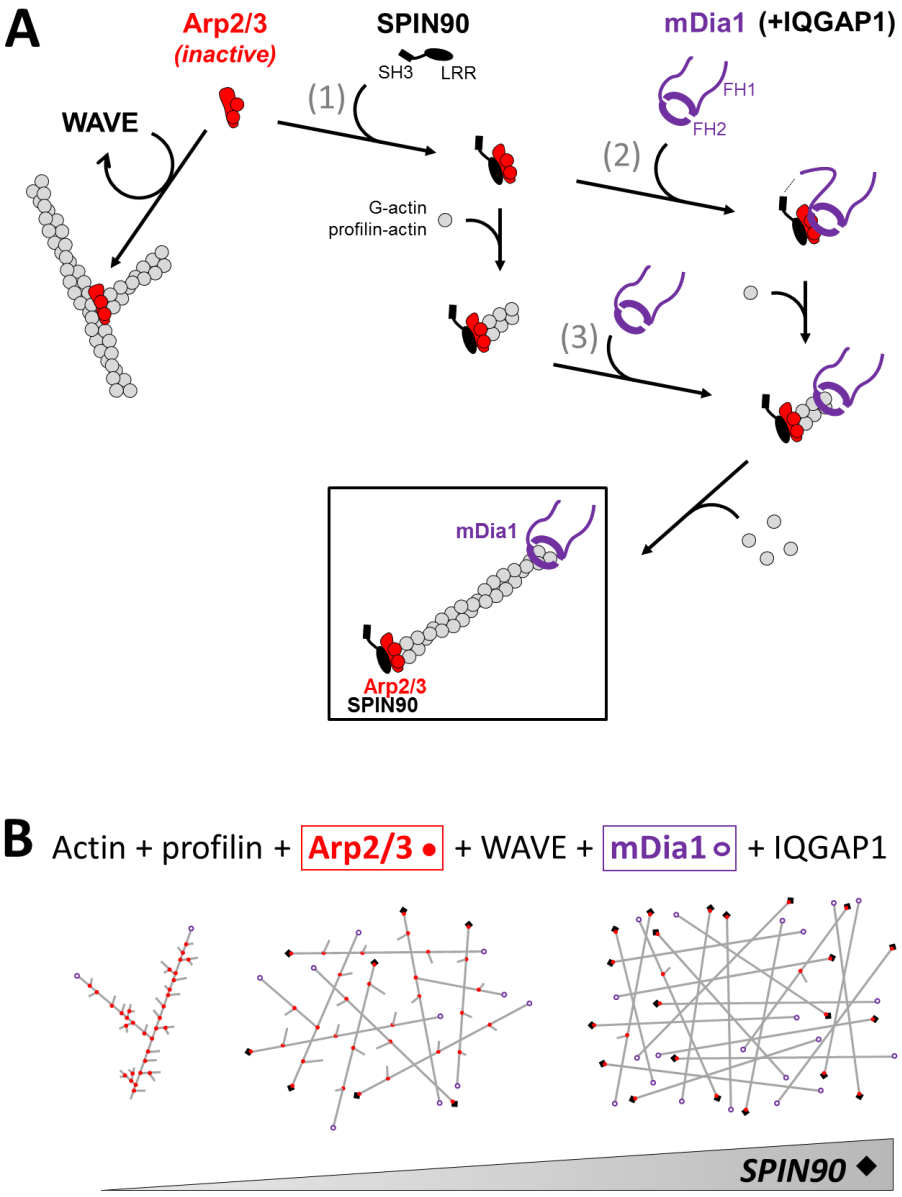

Figure 7. Interplay between SPIN90, mDia1, and Arp2/3 at the filament and network levels. A. Interplay at the molecular level. SPIN90 activates the Arp2/3 complex (reaction 1) to nucleate linear filaments, in competition with Arp2/3 branching (left) following activation by the WAVE complex (not sketched) and binding to the sides of existing filaments. SPIN90 remains bound to the activated Arp2/3 complex at the pointed end of the nucleated filament. Formin mDia1, maintained in an active conformation by IQGAP1 (not sketched), can bind to the filament barbed end and accelerate its elongation using profilin-actin. Barbed ends nucleated by SPIN90-Arp2/3 are particularly prone to binding mDia1 (reaction 3). Formin mDia1 can also bind to the SPIN90-Arp2/3 complex, forming a ternary complex (reaction 2), which efficiently nucleates rapidly growing filaments. Both routes lead to the formation of filaments with mDia1 at their barbed ends and SPIN90-Arp2/3 at their pointed ends. **B**. Interplay at the network level. Increasing the amount of SPIN90 leads to lower branching densities, and favors the generation of linear filaments rapidly elongated by formin mDia1.